Yu-Chen Karen Chen-Wiegart[1]

Department of Materials Science and Engineering,
Stony Brook University,
Stony Brook, NY 11794;
National Synchrotron Light Source II,
Brookhaven National Laboratory,
Upton, NY 11973
e-mail: Karen.Chen-Wiegart@stonybrook.edu

SangSoo Kim

XFEL Beamline Division,
Pohang Accelerator Laboratory,
80 Jigokro-127-beongil, Nam-gu, Pohang,
Gyeongbuk 37673, South Korea
e-mail: sangsookim@postech.ac.kr

David Vine

Sigray,
Concord, CA 94520
e-mail: dvine@sigray.com

Xianghui Xiao

National Synchrotron Light Source II,
Brookhaven National Laboratory,
Upton, NY 11973
e-mail: xiao@bnl.gov

Chonghang Zhao

Department of Materials Science and Engineering,
Stony Brook University,
Stony Brook, NY 11794
e-mail: chonghang.zhao@stonybrook.edu

Mark A. Pfeifer

Cornell Center for Materials Research,
Cornell University,
Ithaca, NY 14853
e-mail: map322@cornell.edu

Garth J. Williams

National Synchrotron Light Source II,
Brookhaven National Laboratory,
Upton, NY 11973
e-mail: gwilliams@bnl.gov

Ian McNulty[1]

MAX IV Laboratory,
Lund University,
Fotongatan 2,
Lund 224 94, Sweden
e-mail: ian.mcnulty@maxiv.lu.se

Revealing Three-Dimensional Morphology in Nanoporous Gold Using Three-Dimensional X-Ray Fresnel Coherent Diffractive Imaging Tomography

Nanoporous metals fabricated by dealloying have a unique bi-continuous, sponge-like porous structure with ultra-high surface area. The unique properties of these materials, especially nanoporous gold, have numerous potential applications in sensors and actuators and in energy-related applications such as catalytic materials, super-capacitors, and battery supports. The degree of porosity and size of the metal ligaments are critical parameters that determine many properties and thus govern the functionalities of nanoporous metals in many applications including energy storage and conversion. We used Fresnel coherent diffractive imaging combined with tomographic reconstruction to quantify the nanoscale three-dimensional spatial distribution and homogeneity of the porosity and ligament size within a bulk sample of nanoporous gold. The average porosity and its standard deviation along the axial direction through the sample were determined, as well as the characteristic feature size and its standard deviation. The result shows that free corrosion is an effective way to create homogeneous nanoporous metals with sample sizes on the order of 1 μm. [DOI: 10.1115/1.4046414]

Keywords: dealloying, FCDI, tomography, nanoporous metal, NPG

1 Introduction

Many important potential applications and intriguing fundamental aspects of nanoporous and bi-continuous metal structures have been discovered in recent years [1–3]. Dealloying is an effective method to fabricate these nanoporous and bi-continuous structures [4] with evolving methods including chemical and electrochemical dealloying [5–7], liquid metal dealloying [8–12], solid-state dealloying [13–15], vapor phase dealloying [16–18], and compound-decomposition dealloying [19]. Applications in energy storage and conversion have also been developed, including lithium ion batteries [20–24], sodium ion batteries [25,26], potassium ion batteries [27], fuel cells [28], super-capacitors [29], and catalysts [30–32].

Among the various nanoporous metallic materials, nanoporous gold (np-Au) prepared by dealloying has attracted great attention due to its range of potential applications [6,33,34]. These include bio-sensors [35–37], surface-chemistry-driven actuators [38], catalysis [39,40], super-capacitors [29], and Li-ion battery anodes [41]. The optical, electrochemical, and mechanical properties of (np-Au),

and its performance in these applications, typically depend strongly on the degree of porosity and size of the gold ligaments. Dealloying by free corrosion is one of the simplest and most widely used methods for fabricating (np-Au). However, a major question raised is whether this approach can result in a homogeneous distribution of the pores. Coarsening of the pores as the dealloying front propagates through the sample can lead to growth of the ligament size, decrease in the porosity, or a combination of both.

Various methods have proven indispensable for studying the morphology of these materials and its relation to functionality including small angle X-ray scattering [42,43] and transmission electron microscopy [44,45]. Scanning electron microscopy (SEM) is generally used to characterize the ligament size and porosity at the surfaces of nanoporous metals. To quantify the ligament size and porosity distribution in bulk specimens of np-Au, an electron-dense, complex, sponge-like three-dimensional (3D) structure, characterization techniques with sufficient penetration and 3D imaging capability are required, in addition to complementary bulk analysis which provides spatially averaged information. Transmission X-ray microscopy (TXM) was used to study coarsening in a thick sample of np-Au in 3D by tomographic methods [46], propagation of the dealloying front during np-Au formation by *in situ* methods [47], and the dependence of dealloying velocity on alloy composition [48]. TXM was also applied to study processing-structure–property correlation in liquid metal dealloying for fabricating nanoporous materials with less noble elements [10,12]. X-ray Bragg coherent diffractive imaging (Bragg CDI) provides the capability to measure lattice displacement and strain filed, and to identify individual grain, and has been applied to study strain evolution in dealloying of nanoporous Au [49,50]. X-ray ptychography has also been applied to analyze np-Au [51,52]. X-ray Fresnel coherent diffractive imaging (FCDI) [53] is similarly well suited to study dense, thick specimens but with a higher spatial resolution than that of the X-ray lenses typically used in transmission X-ray microscopy. Prior work have demonstrated FCDI tomography using a glass capillary as a test object [54]. In this paper, we apply FCDI tomography to quantify the nanoscale porosity, ligament size distribution, and their homogeneity within the interior of a bulk sample of nanoporous gold formed by free corrosion dealloying.

2 Experiment and Analysis Procedures

2.1 Sample Preparation. We prepared the material used to fabricate the nanoporous gold sample by alloying silver and gold with an arc-melting technique into a Ag–30 at% Au alloy ingot, drew the alloy in to a wire of $50\,\mu m$ diameter, cast it within a glass tube, and then thinned an exposed tip of the wire to 0.5–$1\,\mu m$ diameter by focused ion beam milling. We dealloyed the thinned tip to fabricate the nanoporous structure by submerging it in nitric acid (11.7M, 75 vol%, 68–70% assay, in de-ionized

water) for 30 min. A SEM image of the resulting nanoporous gold sample is shown in Fig. 1(*a*).

2.2 Measurement. We imaged the sample by X-ray FCDI at the 2-ID-B beamline [55] at the Advanced Photon Source, Argonne National Laboratory. A coherent X-ray beam with an energy of 2.5 keV (above the Au M5 absorption edge at 2.2 keV) was used to optimize the sample contrast. The sample was placed ~0.6 mm downstream of the focus of a Fresnel zone plate lens with a 50 nm outmost zone width and 16.36 mm focal length. Fresnel coherent diffraction patterns were measured 332 mm downstream of the focus with a charge-coupled device (CCD) camera (2048×2048 pixels with a size of $13.5 \times 13.5\,\mu m$). Further discussion on the FCDI method can be found in prior work [56].

Diffraction patterns were measured at every 5 deg over a 180 deg range of sample projections to collect a tomographic dataset (Figs. 1(*b*) and 1(*c*)). The exact sample distance to the zone plate was determined by fitting a circular pattern to the focus distance from an initial estimate of the reconstruction (from the central holographic region of the diffraction data). Two sets of 100 frames of data were taken at each projection angle. One set was taken with a shorter exposure time (2–2.5 s) to measure the signal at small momentum transfer. The other set was taken with a longer exposure time (7–7.5 s) to measure the higher resolution signal at large momentum transfer. A Kapton attenuator was used for the latter measurement in order to avoid saturating the center of the CCD. A distinctive ring was present around the center of the diffraction patterns, indicating that the sample had a characteristic length. The highest resolution data extend to 0.4 nm^{-1} in reciprocal space. So-called "white-field" data (with the sample removed to measure the incident illumination) and "black-field" data (with the X-ray beam shuttered to measure the CCD background signal) were also collected.

2.3 FCDI Data Reconstruction. Reconstruction of tomographic projections from the Fresnel coherent diffraction patterns involved two steps. First, the complex amplitude of the incident illumination was recovered from the white-field data. Second, phase retrieval of the sample diffraction data was performed to recover the complex transmission function of the nanoporous gold sample, using the algorithm developed by Williams et al. [57]. Using a tight support based on the approximate sample shape as a constraint significantly decreased the number of iterations needed and improved the reproducibility of the reconstructions.

2.4 Tomographic Reconstruction, Segmentation, and Three-Dimensional Structure Analysis. The projections were aligned manually defining a box ($\sim 1\,\mu m \times 1\,\mu m$) centering the tip of the nanoporous gold sample and then shifting the projections pixel by pixel to maximize the correlation coefficient between projections. A standard filtered back-projection algorithm [58] was
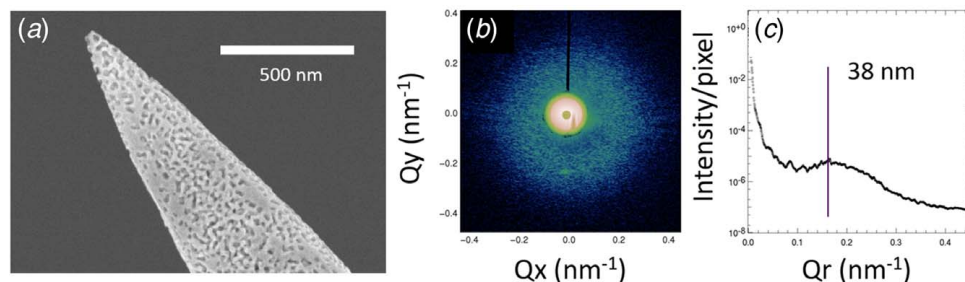
Fig. 1 (*a*) SEM image of the nanoporous gold sample. (*b*) Sample diffraction pattern with the *q*-range indicated in units of nm^{-1}. The pattern is a composite of two different datasets, one obtained at low-*q* and one obtained at high-*q* using a beam stop to block the intense central region of the pattern. (*c*) Power spectral density of the sample transmission function. The peak at 0.16 nm^{-1} corresponds to a most probable pore size of 38 nm.

then applied to the aligned projections to obtain a 3D reconstruction. Segmentation of the reconstructed images was conducted by thresholding and was then applied to a sub-volume (~300 nm × 300 nm × 900 nm) taken from the center of the tomography reconstructed dataset. Cropping into a sub-volume can avoid the surface region that has been slightly damaged by the ion beam during the sample preparation process, as seen in the SEM image (Fig. 1(a)). Within ±8% of theoretical average porosity (70%), different threshold values were chosen. The porosity and the pore size distribution were calculated as a function of position from this volume. The effects of choosing different threshold values to the porosity and pore size will also be discussed in Sec. 3.

The porosity was calculated along the long axis (axial direction) of the sample from the fraction of the occupied volume within the overall sample volume. The pore size was represented by reciprocal of area density (Sv^{-1}), calculated from a triangulated mesh used to approximate the surface. The gold volume fraction (1-porosity) was calculated along the radial direction of the sample.

3 Results and Discussions

3.1 Reconstructed Projections. The reconstructed sample absorption for three representative projection angles through the nanoporous gold sample with a voxel size of 5.9 nm is shown in Figs. 2(a)–2(c). They were calculated from the reconstructed magnitude and phase of the reconstructed transmission function. The tabulated value of $\delta = 3.211 \times 10^{-4}$ was used. The value δ is defined as the real part of the refractive index of the sample for X-rays. The effective field of view is changing as a function of angle due to the fact that the center of the sample tip was not perfectly aligned to the center of rotation, and therefore the region of illumination was changing while rotating the sample. A zoom-in view of Fig. 2(a) was shown in Fig. 2(d). As the method is based on phase retrieval, Fresnel CDI can also provide better phase-contrast image, which can be applied in the future for materials with low absorption contrast.

3.2 Three-Dimensional Reconstruction. A cross section of the reconstructed 3D volume of the sample is shown in Fig. 3(a). The porous nature of the structure is clearly visible (Fig. 3(b)). Figure 3(c) shows the details of the structure after segmentation.

3.3 Porosity Analysis Along the Axial Direction. During the dealloying process, the silver atoms that occupied 70% of the sample volume were dissolved into the nitric acid solution, leaving a nanoporous gold structure with ~70% overall porosity. However, the porosity may have varied within the sample as a result of heterogeneous pore formation. The porosity was calculated from a total of ~160 thin slabs (300 nm × 300 nm × 5.9 nm), with the x–y plane perpendicular to the sample axis (z) and plotted as a function of the distance between the cross-sectional planes to the sample tip (d). The result is shown in Fig. 4 for three different thresholds, which yield an average porosity ranging from 62.3%
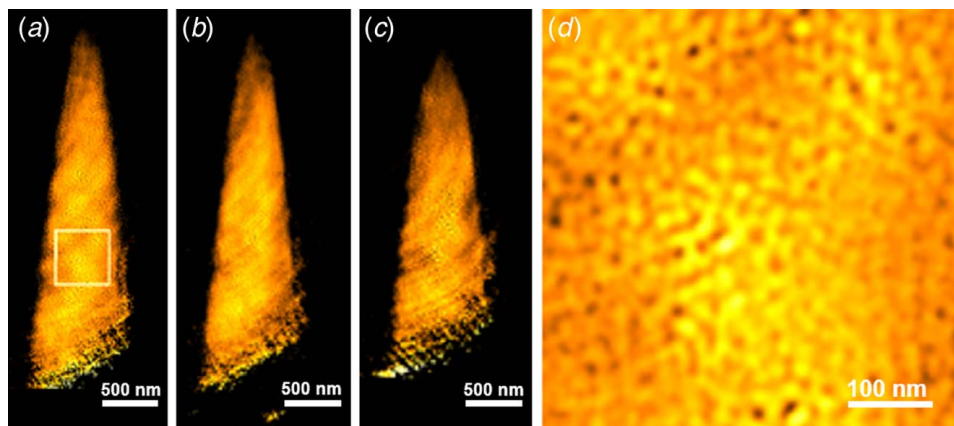

Fig. 2 Sample absorption obtained from the FCDI reconstructions at projection angles of (a) 36 deg, (b) 111 deg, and (c) 186 deg. All the reconstructed projections can be found in supplement materials. (d) A zoomed-in view of (a). The corresponding area is indicated as a square in (a).
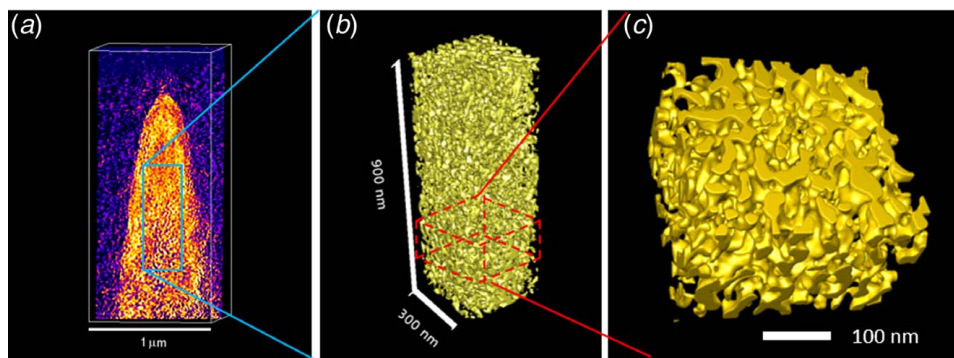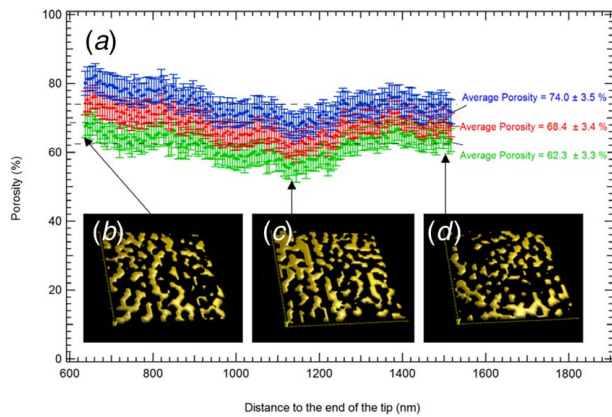

Fig. 3 3D reconstruction of the nanoporous gold sample. (a) Cross section of the entire reconstructed volume. (b) Surface mesh of a smaller volume after segmentation, taken from the entire reconstructed volume shown in (a). (c) Zoomed-in view of (b) for visualization of the structural details. The rectangles in (a) and (b) correspond to the enlarged areas in (b) and (c), respectively.

Fig. 4 (*a*) Porosity of each *x–y* slab (5.9 nm in thickness) as a function of axial distance along the sample. (*b*)–(*d*) Morphology of corresponding sample locations, with thresholding of medium absorption. The cross sections were taken at (*b*) 1516.3 nm, (*c*) 1144.6 nm, and (*d*) 643.1 nm from the tip of the sample. Each image showed a thin slab of 300 nm × 300 nm × 5.9 nm.

to 74.0%. Although the average porosity value depends on the threshold value used for segmentation, the overall trend in the porosity distribution as a function of the position remains unchanged. The insets in Fig. 4 show the nanoporous gold morphology at corresponding sample locations.

3.4 Feature Size Distribution Along the Axial Direction.

The ligament size is an important parameter determining the properties of nanoporous gold, but this can be difficult to define because the porous structure forms an open network. Here, we used the characteristic feature size or area density, S_V, defined to be the gold surface area per sample volume. The reciprocal of the area density, Sv^{-1}, is a good representation of the feature size [46]. We calculated Sv^{-1} as a function of *d* with a volume of ~300 nm × 300 nm × 30 nm at each position *d*. The result is plotted in Fig. 5. A slight decreasing trend was observed in the features size distribution, potentially due to the simultaneous coarsening occurred during the dealloying. However, the variation is small, and the feature size distribution remains relatively homogeneous. The same threshold values were used here as in the porosity calculation. The threshold which results in a higher porosity also gives a higher Sv^{-1}. The
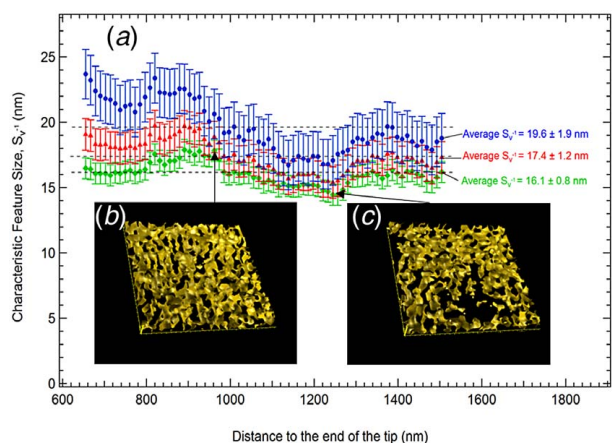
Fig. 5 (*a*) Distribution of the characteristic feature size Sv^{-1} versus axial distance along the sample. (*b*) and (*c*) Surfaces of 300 nm × 300 nm × 30 nm slabs of the sample, with thresholding of medium absorption at (*b*) 1256.7 nm and (*c*) 690.9 nm from the tip of the sample.

Table 1 Summary of the average porosity, characteristic feature size, and their standard deviations as a function of position within the sample

Thresholding	Porosity ± standard deviation (%)	Characteristic feature size, Sv^{-1} ± standard deviation (nm)
Lower absorption	62.3 ± 3.3	16.1 ± 0.8
Medium absorption	68.4 ± 3.4	17.4 ± 1.2
Higher absorption	74.0 ± 3.5	19.6 ± 1.9

insets in Fig. 5 show the sample surface at the positions corresponding to the maximum and minimum characteristic feature sizes, Sv^{-1}, respectively.

The average threshold value, porosity, and the pore size are summarized in Table 1. Regardless of how the porosity and ligament size depend on the threshold value, the standard deviations of their values from the average as a function of axial position remains small, 3.3–3.5% for the porosity and 0.8–1.9 nm for the ligament size. This result shows that, independent of any rearrangement of the gold atoms and coarsening during the dealloying process, the porosity and the ligament size distributions are nearly homogeneous throughout the sample with only slight variation. Analysis on sample with larger size could be conducted in the future to further understand if there is limitation of long-range mass transport in the dealloying process that could lead to morphological heterogeneity.

4 Summary

We used Fresnel CDI to image a nanoporous gold sample with diameter ~500 nm and height ~1.5 μm. Diffraction patterns collected at every 5 deg were reconstructed into projections of the sample absorption, which were then reconstructed into a 3D volume by tomographic methods. We calculated the porosity and ligament size distribution as a function of axial sample position from thin slabs extracted from the reconstructed 3D sample volume. Small variations in these parameters indicate that the free corrosion can be used to fabricate nanoporous gold with a nearly homogeneous pore distribution. This analysis provides valuable insight for developing devices including sensors and actuators and for energy-related applications such as catalysts, super-capacitors, and battery supports based on this material. In the future, Fresnel CDI with smaller angular step size for higher resolution characterization would be important to provide better 3D analysis. Future work can also utilize ptychographic tomography to further investigate the 3D morphology of materials fabricated by dealloying for energy-related applications.

References

[1] Tappan, B. C., Steiner, S. A., and Luther, E. P., 2010, "Nanoporous Metal Foams," Angew. Chem. Int. Ed., 49(27), pp. 4544–4565.

[2] Ding, Y., and Chen, M. W., 2009, "Nanoporous Metals for Catalytic and Optical Applications," MRS Bull., 34(8), pp. 569–576.

[3] Weissmüller, J., Newman, R. C., Jin, H. J., Hodge, A. M., and Kysar, J. W., 2009, "Nanoporous Metals by Alloy Corrosion: Formation and Mechanical Properties," MRS Bull., 34(8), pp. 577–586.

[4] McCue, I., Benn, E., Gaskey, B., and Erlebacher, J., 2016, "Dealloying and Dealloyed Materials," Annu. Rev. Mater. Res., 46(1), pp. 263–286.

[5] Chen, Q., and Sieradzki, K., 2013, "Mechanisms and Morphology Evolution in Dealloying," J. Electrochem. Soc., 160(6), pp. C226–C231.

[6] Erlebacher, J., Aziz, M. J., Karma, A., Dimitrov, N., and Sieradzki, K., 2001, "Evolution of Nanoporosity in Dealloying," Nature, 410(6827), pp. 450–453.

[7] Erlebacher, J., and Sieradzki, K., 2003, "Pattern Formation During Dealloying," Scr. Mater., 49(10), pp. 991–996.

[8] Geslin, P. A., McCue, I., Gaskey, B., Erlebacher, J., and Karma, A., 2015, "Topology-Generating Interfacial Pattern Formation During Liquid Metal Dealloying," Nat. Commun., 6(1), p. 8.

[9] McCue, I., Gaskey, B., Geslin, P. A., Karma, A., and Erlebacher, J., 2016, "Kinetics and Morphological Evolution of Liquid Metal Dealloying," Acta Mater., 115, pp. 10–23.

[10] Zhao, C., Wada, T., De Andrade, V., Williams, G. J., Gelb, J., Li, L., Thieme, J., Kato, H., and Chen-Wiegart, Y.-C. K., 2017, "Three-Dimensional Morphological and Chemical Evolution of Nanoporous Stainless Steel by Liquid Metal Dealloying," ACS Appl. Mater. Interfaces, 9(39), pp. 34172–34184.

[11] Wada, T., Yubuta, K., Inoue, A., and Kato, H., 2011, "Dealloying by Metallic Melt," Mater. Lett., 65(7), pp. 1076–1078.

[12] Chen-Wiegart, Y. C. K., Wada, T., Butakov, N., Xiao, X. H., De Carlo, F., Kato, H., Wang, J., Dunand, D. C., and Maire, E., 2013, "3D Morphological Evolution of Porous Titanium by X-Ray Micro- and Nano-Tomography," J. Mater. Res., 28(17), pp. 2444–2452.

[13] Wada, T., Yubuta, K., and Kato, H., 2016, "Evolution of a Bicontinuous Nanostructure via a Solid-State Interfacial Dealloying Reaction," Scr. Mater., 118, pp. 33–36.

[14] McCue, I., and Demkowicz, M. J., 2017, "Alloy Design Criteria for Solid Metal Dealloying of Thin Films," JOM, 69(11), pp. 2199–2205.

[15] Zhao, C. H., Kisslinger, K., Huang, X. J., Lu, M., Camino, F., Lin, C. H., Yan, H. F., Nazaretski, E., Chu, Y., Ravel, B., Liu, M. Z., and Chen-Wiegart, Y. C. K., 2019, "Bi-Continuous Pattern Formation in Thin Films via Solid-State Interfacial Dealloying Studied by Multimodal Characterization," Mater. Horiz., 6(10), pp. 1991–2002.

[16] Han, J. H., Li, C., Lu, Z., Wang, H., Wang, Z. L., Watanabe, K., and Chen, M. W., 2019, "Vapor Phase Dealloying: A Versatile Approach for Fabricating 3D Porous Materials," Acta Mater., 163, pp. 161–172.

[17] Lu, Z., Li, C., Han, J. H., Zhang, F., Liu, P., Wang, H., Wang, Z. L., Cheng, C., Chen, L. H., Hirata, A., Fujita, T., Erlebacher, J., and Chen, M. W., 2018, "Three-Dimensional Bicontinuous Nanoporous Materials by Vapor Phase Dealloying," Nat. Commun., 9(1), pp. 1–7.

[18] Sun, Y. X., and Ren, Y. B., 2015, "New Preparation Method of Porous Copper Powder Through Vacuum Dealloying," Vacuum, 122, pp. 215–217.

[19] Chen, Q., 2014, "Bi-Continuous Nanoporous Structure Formation via Compound Decomposition," J. Electrochem. Soc., 161(10), pp. H643–H646.

[20] Zhao, C. H., Wada, T., De Andrade, V., Gursoy, D., Kato, H., and Chen-Wiegart, Y. C. K., 2018, "Imaging of 3D Morphological Evolution of Nanoporous Silicon Anode in Lithium Ion Battery by X-Ray Nano-Tomography," Nano Energy, 52, pp. 381–390.

[21] Wada, T., Yamada, J., and Kato, H., 2016, "Preparation of Three-Dimensional Nanoporous Si Using Dealloying by Metallic Melt and Application as a Lithium-Ion Rechargeable Battery Negative Electrode," J. Power Sources, 306, pp. 8–16.

[22] Saager, S., Scheffel, B., Zywitzki, O., Modes, T., Piwko, M., Doerfler, S., Althues, H., and Metzner, C., 2019, "Porous Silicon Thin Films as Anodes for Lithium Ion Batteries Deposited by Co-Evaporation of Silicon and Zinc," Surf. Coat. Technol., 358, pp. 586–593.

[23] Cook, J. B., Detsi, E., Liu, Y. J., Liang, Y. L., Kim, H. S., Petrissans, X., Dunn, B., and Tolbert, S. H., 2017, "Nanoporous Tin With a Granular Hierarchical Ligament Morphology as a Highly Stable Li-Ion Battery Anode," ACS Appl. Mater. Interfaces, 9(1), pp. 293–303.

[24] Wada, T., Ichitsubo, T., Yubuta, K., Segawa, H., Yoshida, H., and Kato, H., 2014, "Bulk-Nanoporous-Silicon Negative Electrode With Extremely High Cyclability for Lithium-Ion Batteries Prepared Using a Top-Down Process," Nano Lett., 14(8), pp. 4505–4510.

[25] Detsi, E., Petrissans, X., Yan, Y., Cook, J. B., Deng, Z. L., Liang, Y. L., Dunn, B., and Tolbert, S. H., 2018, "Tuning Ligament Shape in Dealloyed Nanoporous Tin

[26] and the Impact of Nanoscale Morphology on Its Applications in Na-Ion Alloy Battery Anodes," Phys. Rev. Mater., 2(5), p. 055404.

[26] Li, H. M., Wang, K. L., Zhou, M., Li, W., Tao, H. W., Wang, R. X., Cheng, S. J., and Jiang, K., 2019, "Facile Tailoring of Multidimensional Nanostructured Sb for Sodium Storage Applications," ACS Nano, 13(8), pp. 9533–9540.

[27] Sang, Z. Y., Su, D., Wang, J. S., Liu, Y., and Ji, H. M., 2020, "Bi-Continuous Nanoporous Carbon Sphere Derived From SiOC as High-Performance Anodes for PIBs," Chem. Eng. J., 381, p. 122677.

[28] Snyder, J., Fujita, T., Chen, M. W., and Erlebacher, J., 2010, "Oxygen Reduction in Nanoporous Metal—Ionic Liquid Composite Electrocatalysts," Nat. Mater., 9(11), pp. 904–907.

[29] Lang, X. Y., Hirata, A., Fujita, T., and Chen, M. W., 2011, "Nanoporous Metal/Oxide Hybrid Electrodes for Electrochemical Supercapacitors," Nat. Nanotechnol., 6(4), pp. 232–236.

[30] Wittstock, A., Zielasek, V., Biener, J., Friend, C. M., and Baumer, M., 2010, "Nanoporous Gold Catalysts for Selective Gas-Phase Oxidative Coupling of Methanol at Low Temperature," Science, 327(5963), pp. 319–322.

[31] Chatterjee, S., Griego, C., Hart, J. L., Li, Y. W., Taheri, M. L., Keith, J., and Snyder, J. D., 2019, "Free Standing Nanoporous Palladium Alloys as CO Poisoning Tolerant Electrocatalysts for the Electrochemical Reduction of CO2 to Formate," ACS Catal., 9(6), pp. 5290–5301.

[32] Chen, J. Y., Li, Y., Lu, N. L., Tian, C. H., Han, Z. D., Zhang, L., Fang, Y., Qian, B., Jiang, X. F., and Cui, R. J., 2018, "Nanoporous PdCe Bimetallic Nanocubes With High Catalytic Activity Towards Ethanol Electro-Oxidation and the Oxygen Reduction Reaction in Alkaline Media," J. Mater. Chem. A, 6(46), pp. 23560–23568.

[33] Kertis, F., Snyder, J., Govada, L., Khurshid, S., Chayen, N., and Erlebacher, J., 2010, "Structure/Processing Relationships in the Fabrication of Nanoporous Gold," JOM, 62(6), pp. 50–56.

[34] Graf, M., Roschning, B., and Weissmuller, J., 2017, "Nanoporous Gold by Alloy Corrosion: Method-Structure–Property Relationships," J. Electrochem. Soc., 164(4), pp. C194–C200.

[35] Zheng, Y. J., Xu, Y. C., Lin, L. L., Li, Y., Chen, W., Chen, J. Y., Lei, Y., Lin, L. Q., Liu, A. L., Lin, X. H., and Weng, S. H., 2019, "Nanoporous Gold Electrode Prepared From Two-Step Square Wave Voltammetry (SWV) and Its Application for Electrochemical DNA Biosensing of Lung Resistance Related Protein (LRP) Gene," J. Electroanal. Chem., 840, pp. 165–173.

[36] Kafi, A. K. M., Ahmadalinezhad, A., Wang, J. P., Thomas, D. F., and Chen, A. C., 2010, "Direct Growth of Nanoporous Au and Its Application in Electrochemical Biosensing," Biosens. Bioelectron., 25(11), pp. 2458–2463.

[37] Qiu, H. J., Xue, L. Y., Ji, G. L., Zhou, G. P., Huang, X. R., Qu, Y. B., and Gao, P. J., 2009, "Enzyme-Modified Nanoporous Gold-Based Electrochemical Biosensors," Biosens. Bioelectron., 24(10), pp. 3014–3018.

[38] Biener, J., Wittstock, A., Zepeda-Ruiz, L. A., Biener, M. M., Zielasek, V., Kramer, D., Viswanath, R. N., Weissmuller, J., Baumer, M., and Hamza, A. V., 2009, "Surface-Chemistry-Driven Actuation in Nanoporous Gold," Nat. Mater., 8(1), pp. 47–51.

[39] Xu, C., Xu, X., Su, J., and Ding, Y., 2007, "Research on Unsupported Nanoporous Gold Catalyst for CO Oxidation," J. Catal., 252(2), pp. 243–248.

[40] Graf, M., Haensch, M., Carstens, J., Wittstock, G., and Weissmuller, J., 2017, "Electrocatalytic Methanol Oxidation With Nanoporous Gold: Microstructure and Selectivity," Nanoscale, 9(45), pp. 17839–17848.

[41] Yu, Y., Gu, L., Lang, X. Y., Zhu, C. B., Fujita, T., Chen, M. W., and Maier, J., 2011, "Li Storage in 3D Nanoporous Au-Supported Nanocrystalline Tin," Adv. Mater., 23(21), pp. 2443–2447.

[42] Schofield, E. J., Ingham, B., Turnbull, A., Toney, M. F., and Ryan, M. P., 2008, "Strain Development in Nanoporous Metallic Foils Formed by Dealloying," Appl. Phys. Lett., 92(4), p. 043118.

[43] Dixon, M. C., Daniel, T. A., Hieda, M., Smilgies, D. M., Chan, M. H. W., and Allara, D. L., 2007, "Preparation, Structure, and Optical Properties of Nanoporous Gold Thin Films," Langmuir, 23(5), pp. 2414–2422.

[44] Fujita, T., Qian, L. H., Inoke, K., Erlebacher, J., and Chen, M. W., 2008, "Three-Dimensional Morphology of Nanoporous Gold," Appl. Phys. Lett., 92(25), pp. 251902.

[45] Rosner, H., Parida, S., Kramer, D., Volkert, C. A., and Weissmuller, J., 2007, "Reconstructing a Nanoporous Metal in Three Dimensions: An Electron Tomography Study of Dealloyed Gold Leaf," Adv. Eng. Mater., 9(7), pp. 535–541.

[46] Chen, Y. C. K., Chu, Y. S., Yi, J., McNulty, I., Shen, Q., Voorhees, P. W., and Dunand, D. C., 2010, "Morphological and Topological Analysis of Coarsened Nanoporous Gold by X-Ray Nanotomography," Appl. Phys. Lett., 96(4), p. 043122.

[47] Chen-Wiegart, Y. C. K., Wang, S., Lee, W. K., McNulty, I., Voorhees, P. W., and Dunand, D. C., 2013, "In-Situ Imaging of Dealloying During Nanoporous Gold Formation by Transmission X-Ray Microscopy," Acta Mater., 61(4), pp. 1118–1125.

[48] Chen-Wiegart, Y. C. K., Wang, S., McNulty, I., and Dunand, D. C., 2013, "Effect of Ag–Au Composition and Acid Concentration on Dealloying Front Velocity and Cracking During Nanoporous Gold Formation," Acta Mater., 61(15), pp. 5561–5570.

[49] Chen-Wiegart, Y. C. K., Harder, R., Dunand, D. C., and McNulty, I., 2017, "Evolution of Dealloying Induced Strain in Nanoporous Gold Crystals," Nanoscale, 9(17), pp. 5686–5693.

[50] Cha, W., Liu, Y. H., You, H., Stephenson, G. B., and Ulvestad, A., 2017, "Dealloying in Individual Nanoparticles and Thin Film Grains: A Bragg Coherent Diffractive Imaging Study," Adv. Funct. Mater., 27(25), p. 1700331.

[51] Baier, S., Damsgaard, C. D., Scholz, M., Benzi, F., Rochet, A., Hoppe, R., Scherer, T., Shi, J. J., Wittstock, A., Weinhausen, B., Wagner, J. B., Schroer,

C. G., and Grunwaldt, J. D., 2016, "In Situ Ptychography of Heterogeneous Catalysts Using Hard X-Rays: High Resolution Imaging at Ambient Pressure and Elevated Temperature," Microsc. Microanal., **22**(1), pp. 178–188.

[52] Fam, Y., Sheppard, T. L., Diaz, A., Scherer, T., Holler, M., Wang, W., Wang, D., Brenner, P., Wittstock, A., and Grunwaldt, J. D., 2018, "Correlative Multiscale 3D Imaging of a Hierarchical Nanoporous Gold Catalyst by Electron, Ion and X-Ray Nanotomography," Chemcatchem, **10**(13), pp. 2858–2867.

[53] Abbey, B., Nugent, K. A., Williams, G. J., Clark, J. N., Peele, A. G., Pfeifer, M. A., De Jonge, M., and McNulty, I., 2008, "Keyhole Coherent Diffractive Imaging," Nat. Phys., **4**(5), pp. 394–398.

[54] Putkunz, C. T., Pfeifer, M. A., Peele, A. G., Williams, G. J., Quiney, H. M., Abbey, B., Nugent, K. A., and McNulty, I., 2010, "Fresnel Coherent Diffraction Tomography," Opt. Express, **18**(11), pp. 11746–11753.

[55] McNulty, I., Khounsary, A., Feng, Y. P., Qian, Y., Barraza, J., Benson, C., and Shu, D., 1996, "A Beamline for 1–4 keV Microscopy and Coherence Experiments at the Advanced Photon Source," Rev. Sci. Instrum., **67**(9), p. 3372.

[56] Kim, S., Chen, Y. K., Putkunz, C. T., Dunand, D. C., and McNulty, I., 2010, "Use of justified constraints in coherent diffractive imaging," 10th International Conference on X-ray Microscopy, Chicago, IL, Aug. 15–20, pp. 441–444.

[57] Williams, G. J., Quiney, H. M., Dhal, B. B., Tran, C. Q., Nugent, K. A., Peele, A. G., Paterson, D., and de Jonge, M. D., 2006, "Fresnel Coherent Diffractive Imaging," Phys. Rev. Lett., **97**(2), p. 025506.

[58] Natterer, F., 1986, *The Mathematics of Computerized Tomography*, Vieweg + Teubner Verlag, Weinheim.